Mechanical Systems and Signal Processing 244 (2026) 113770

Contents lists available at ScienceDirect

Mechanical Systems and Signal Processing

journal homepage: www.elsevier.com/locate/ymssp

Short communication

Domino-inspired energy harvesting system (DiEHS) with modular interlocking mechanism for reliable self-powered applications

Zeye Sun [a,b], Yizhou Li [b], Yihao Li [b,c], Chengyun Du [b], Junlei Wang [a,*], Guobiao Hu [b,*]

[a] School of Mechanical and Power Engineering, Zhengzhou University, Zhengzhou 450001, China
[b] Internet of Things Thrust, The Hong Kong University of Science and Technology (Guangzhou), 511455, China
[c] Department of Mechanical and Mechatronics Engineering, The University of Auckland, Auckland 1010, New Zealand

ARTICLE INFO

Keywords:
Energy harvesting
Domino-inspired mechanism
Buckling beam
Modular design
Self-powered IoT devices

ABSTRACT

With the rapid expansion of 5G technology, the growth of Internet of Things (IoT) devices and wireless sensors is advancing at an unprecedented pace, and their low power demands have stimulated advances in energy harvesting technologies. Inspired by the dynamics of dominoes, we propose a modular, interlocking mechanical energy harvester (MIMEH) that integrates a buckling beam with an electromagnetic power-generation unit. Parametric analysis of a single MIMEH module showed that increased beam thickness and indentation distance can boost voltage output by enhancing stored potential energy. When multiple modules are assembled into a modular array, a domino-inspired energy harvesting system (DiEHS) is obtained, with its voltage output scaling with the number of modules. Notably, the DiEHS array displayed contrasting behaviors: voltage amplification along the propagation path under low-energy input, and voltage attenuation under high-energy input. Nevertheless, the harvested energy by the DiEHS remains relatively stable across conditions, safeguarded by the bistable mechanism. The system's practicality was validated by powering an IoT node, highlighting its promise for distributed sensing applications.

1. Introduction

Dominoes, arranged upright in series, can produce a cascading toppling effect once an initial trigger is applied [1]. This phenomenon is a mechanical chain reaction in which gravitational potential energy is sequentially converted into kinetic energy and then transferred from one tile to the next [2]. This process is propagated sequentially, giving rise to a chain reaction. The process depends critically on the spacing, geometry, and friction: each falling domino must strike its neighbor at an effective angle, while surface friction prevents slipping and ensures consistent motion. With these conditions satisfied, the initial disturbance propagates through the sequence, resulting in a cascading fall [3,4].

The domino effect represents a prototypical chain-triggered process, where energy released by a falling unit propagates to its neighbor, resulting in the sequential transfer of energy [5]. This cascading dynamic is analogous to a discrete form of transition waves in waveguides and typically occurs in systems capable of switching between multiple stable equilibrium states [6,7]. In engineered designs, such wave behaviors can be designed and controlled by tuning the stability and interactions of local units, thereby enabling directional energy transport and high-efficiency conversion [8–10].

Bistable elements are central to this process, as their unique properties allow them to store, release, and regulate mechanical energy

* Corresponding authors.
E-mail addresses: jlwang@zzu.edu.cn (J. Wang), guobiaohu@hkust-gz.edu.cn (G. Hu).

https://doi.org/10.1016/j.ymssp.2025.113770
Received 13 October 2025; Received in revised form 3 December 2025; Accepted 14 December 2025
Available online 21 December 2025

[11–13]. By arranging such bistable units along a path and equipping them with harvesting modules, transient mechanical inputs can be effectively harvested and converted into stable electrical outputs. Bistable and multistable energy-harvesting metamaterials, through their engineered potential-energy landscapes, can not only sustain broadband responses but also deliver robust outputs under transient or impulsive disturbances, thereby enhancing their adaptability [14–17]. With the rapid deployment and expansion of 5G networks, IoT devices and wireless sensors are experiencing unprecedented growth [18–20]. Breakthroughs in ultra-low power electronics have opened the possibility of using vibration energy harvesters in place of traditional batteries [21–27]. With the outputs ranging from milliwatts to microwatts, these harvesters can now meet the modest power requirements of such devices. To further accommodate the diverse power requirements of various IoT systems, modular energy harvesters offer tunable output capacities via series or parallel configurations, while also providing flexible integration options for distributed IoT nodes [28,29]. As a result, self-powered IoT nodes based on energy harvesting technologies are increasingly being deployed in real-world applications [30–33], highlighting their practical potential. Building on this momentum, energy harvesting systems inspired by the domino effect present a promising approach to address emerging power supply challenges.

This study adopts the domino-inspired physical mechanism as the foundation for an energy harvesting scheme, as shown in Fig. 1 (a). On this basis, we propose a modular, interlocking mechanical energy harvester (MIMEH) that acts as the functional “tile” in a domino-inspired energy harvesting system (DiEHS). Each MIMEH incorporates a bistable buckling beam with a pair of magnets and is clamped by two symmetric shells embedded with identical coils, as illustrated in Fig. 1(b). The bistable buckling beam enables conversion between potential and kinetic energy, resembling the conversion observed in toppling dominoes. The shells are fabricated by 3D printing and include preset mounting holes to precisely control the indentation distance of the buckling beam. The shell notches enable easy assembly of the MIMEHs. Interconnected MIMEH modules form a DiEHS, as illustrated in Fig. 1(c). Adjacent modules in the DiEHS employ magnets arranged in an NSNS-SNSN pattern (N and S denoting north and south magnetic poles), creating repulsive interactions that facilitate the transfer of perturbations throughout the system. Once a MIMEH is activated, the external perturbation propagates to its neighbor via magnetic repulsion, resembling the domino-like sequential toppling process. The feasibility of the proposed DiEHS was validated through systematic assessments, with its practicality further demonstrated by powering an IoT node, emphasizing its potential in sensing applications.

2. System overview

As illustrated in Fig. 1(c), all bistable units in the DiEHS are initially configured in the same stable state. A non-contact trigger, consisting of a magnet pair identical to those used in the DiEHS, is positioned in front of the first module with like poles facing each

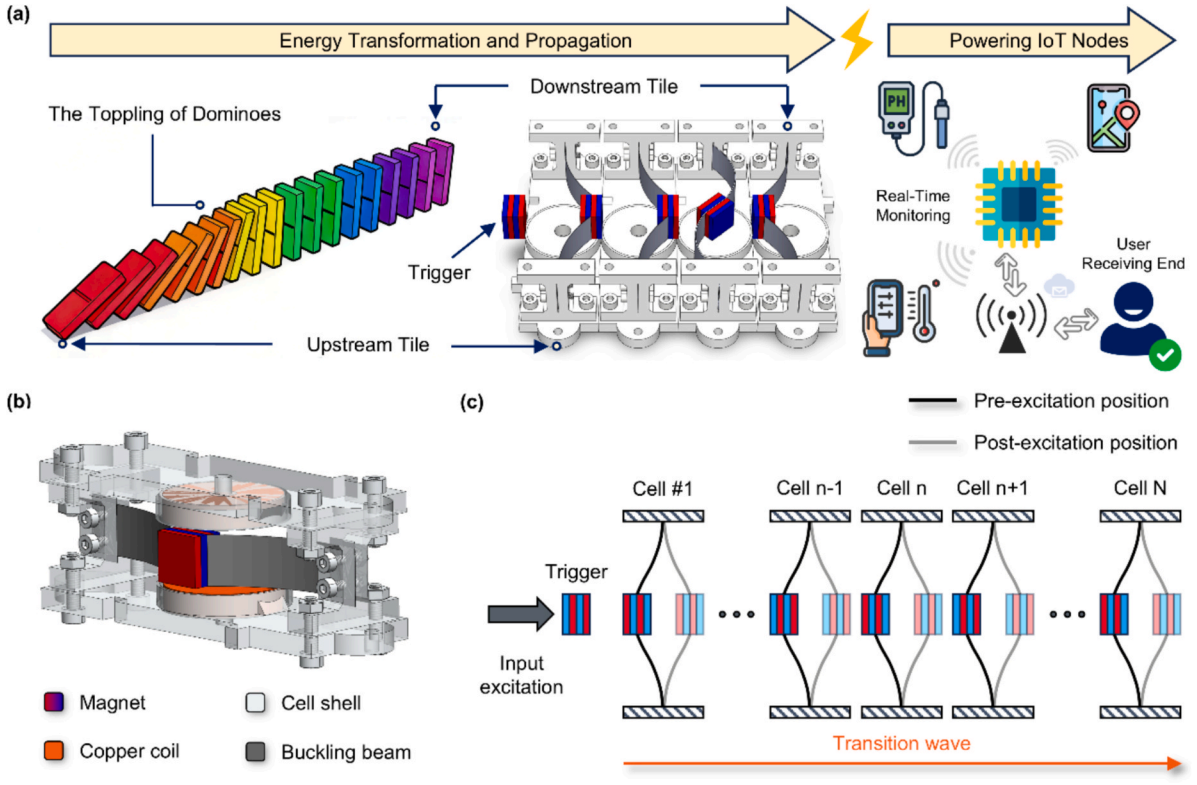

Fig. 1. (a) Conceptual illustration of the DiEHS powering IoT nodes. (b) 3D model of the modular interlocking mechanical energy harvester (MIMEH). (c) Schematic of the DiEHS conducting sequential propagation.

other. The NSNS–SNSN magnetic configuration between the trigger and the first MIMEH, as well as between adjacent modules, establishes repulsive interactions and enables directional transmission of mechanical energy along the chain. When the trigger magnet approaches the first MIMEH, magnetic repulsion initiates the DiEHS, producing a sequential response analogous to the toppling of dominoes. Although the buckling beam undergoes 3D deformation, its in-plane deformation is negligible compared to the out-of-plane response. Hence, the DiEHS can be approximated as a 1D system. The force profile for each MIMEH can be expressed as [8]:

$$m\ddot{x}_n + \alpha\dot{x}_n + F_{coup,n} + \beta\dot{\phi}(x_n) = 0 \tag{1}$$

where m denotes the mass of the magnet pair, x_n is the displacement of the magnet in the n-th module, α is the damping coefficient, and $F_{coup,n}$ denotes the magnetic coupling force exerted on the n-th unit by its neighbors:

$$F_{coup,n} = F_{mag}\left(d_{n+1,n}\right) - F_{mag}\left(d_{n,n-1}\right) \tag{2}$$

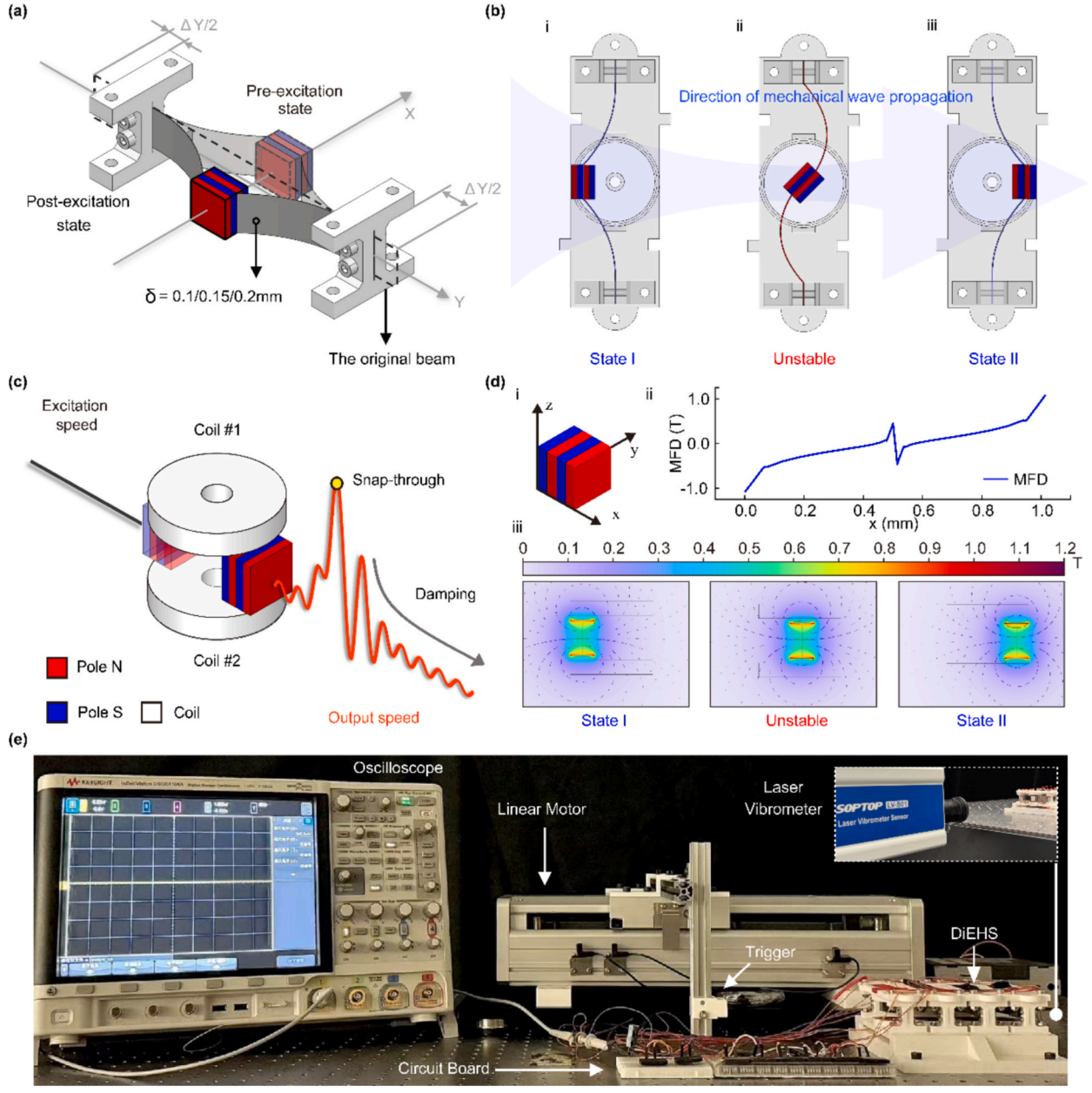

Fig. 2. (a) Schematic of the bistable buckling beam. (b) Snap-through process of the buckling beam. (c) Velocity profile of the magnet during snap-through. (d) Magnetic field distribution during the magnet's leap. (e) Experimental platform for evaluating the DiEHS.

where $d_{n+1,n}$ denotes the center-to-center distance between adjacent magnets, expressed as:

$$d_{n+1,n} = x_{n+1} - x_n + L \tag{3}$$

with L represents the distance between magnets. The upstream distance $d_{n,n\text{-}1}$ is defined analogously. The repulsive magnetic force $F_{mag}()$ is obtained by fitting the measured force–displacement curve for the NSNS-SNSN configuration using an optimal function:

$$F_{mag}(d) = Ad^p \tag{4}$$

where A and p are fitting parameters. The experimental force–displacement data and corresponding fit are provided in Supplementary Fig. S1. And $\beta\phi(x_n)$ represents the bistable potential energy term associated with the buckling beam. The restoring force is expressed as:

$$F_r = -\dot{\phi}(x_n) = -2C_2x_n - 3C_3x_n^2 - 4C_4x_n^3 \tag{5}$$

where C_i are the constants determined by fitting to measured data. The static force–displacement profiles of all bistable configurations examined in this work are shown in Supplementary Fig. S2.

Because each MIMEH incorporates a geometrically symmetric bistable buckling beam, the snap-through transition from state I to state II naturally prepares the module for an immediate reverse transition once the excitation direction is reversed. This structural symmetry ensures that the DiEHS can be reactivated under reciprocating or repeated disturbances without requiring any mechanical resetting.

3. Working mechanism and performance characterization

The non-convex nature of the potential energy provides the system with unstable states. Upon external excitation, the bistable MIMEH conducts a spontaneous transition and snaps from one equilibrium state to the other. This snap-through phenomenon is commonly observed in prestressed buckling structures. The energy conversion unit, as shown in Fig. 2(a), is composed of a prestressed steel strip (quenched 65Mn spring steel) and two identical N52 magnets. The beam is axially compressed by $\Delta Y/2$ at each end (total compression ΔY), forming a buckled configuration with two stable equilibria. All intermediate positions are unstable and cannot be sustained. When external excitation exceeds the restoring force, the buckling beam snaps rapidly from state I to state II, as illustrated in Fig. 2(b).

Due to minor misalignments and fabrication tolerances in the bistable element, the magnet motion exhibits both translational and rotational components. From an energy perspective, the rapid snap-through process converts the potential energy stored in the buckling beam into the kinetic energy of the magnets. The magnet velocity rises sharply, reaching its maximum before decreasing, as illustrated in Fig. 2(c). Once the magnets settle into the stable state II, structural constraints prevent further movement, leading to high-frequency small-amplitude oscillations around the equilibrium position. Energy is gradually dissipated through these oscillations until the system reaches rest. The pronounced velocity surge during snap-through ensures that the MIMEH can produce dependable voltage output, even under low excitations. This effect stems from the rapid velocity change, which intensifies magnetic flux variation in the coils and reinforces electromagnetic induction. The simulated magnetic field distribution, as shown in Fig. 2(d), illustrates the passage of the magnets through the coils.

The geometric parameters of the MIMEH are listed Table 1. To elucidate the influence of design parameters, its performance was systematically characterized by varying the thickness and indentation distance of the buckling beam, which directly govern the stored potential energy and snap-through dynamics, and thus voltage output. Using the optimal parameters, four identical MIMEH units were assembled to form a DiEHS for the subsequent performance evaluation.

Fig. 2(e) presents the experimental setup used to assess the performance of the DiEHS. All experiments were conducted at an ambient room temperature of 23 ± 1 °C on an optical vibration-isolation platform, which effectively suppressed environmental vibrations and external mechanical noise to provide stable measurement conditions. To enhance alignment accuracy and minimize

Table 1
Geometric parameters of the MIMEH.

Description	Symbol	Value
Original beam length	l_0	110 mm
Beam width	δ	15 mm
Beam thickness	t	0.1/ 0.15/ 0.2 mm
Buckling beam length	l	107/ 108/ 109 mm
Magnet length (width)	l_m	15 mm
Magnet thickness	t_m	5 mm
Coil diameter	D	35 mm
Wire diameter	c	0.12 mm
Turns of coil	n	4000
Coil internal resistance	R_0	424.5 Ω
PLA shell length	l_s	130 mm
PLA shell width	b_s	39 mm
PLA shell thickness	t_s	6 mm

gravity-induced potential-well asymmetry, the prototype was mounted on the platform using a custom 3D-printed fixture. A magnetic trigger, mounted on an aluminum fixture attached to the slider, was driven by the linear motor to provide controlled and repeatable excitations to initiate the response of the target MIMEH. The triggering response and voltage output of both a single MIMEH and the assembled DiEHS were measured under two excitation modes: quasi-static and constant-velocity excitations. The voltage output was recorded in real time using an oscilloscope (KEYSIGHT InfiniiVision DSOX4104A). A laser Doppler vibrometer (SOPTOP LV-S01) was utilized to calibrate the trigger and to measure the instantaneous magnet velocity during snap-through.

Fig. 3 illustrates the effects of beam thickness (δ, mm) and indentation distance (ΔY, mm) on the voltage output of the MIMEH under different excitation velocities (v_{in}, m/s). The panels are arranged with δ increasing from bottom to top and ΔY increasing from left to right. The first stage features a sharp voltage peak (V_{peak}, V) generated by the rapid snap-through of the magnets, representing the primary energy contribution. After snap-through, the buckling beam settles into a new stable equilibrium, where the fixed ends and geometric constraints restrict further magnet motion to small oscillations around the stable position. These oscillations decay over time due to damping until both the magnets and the buckling beam come to rest. At this stage, the total restoring force of the MIMEH no longer follows a linear dependence on displacement, leading to non-ideal harmonic motion and non-sinusoidal voltage waveforms. As the excitation velocity increases, the mechanical input energy delivered to the MIMEH also increases. Apart from the portion of energy required to overcome the potential barrier of the bistable structure, the remaining input energy is converted into the kinetic energy of the moving magnets, resulting in faster snap-through transitions of the buckling beam. The enhanced magnet motion increases the rate of magnetic flux variation through the coils, thereby generating higher induced voltages. During the rapid snap-through process, the velocity profiles of the magnets resemble the voltage profiles, as illustrated in Supplementary Fig. S3.

Both increasing the thickness of the buckling beam and enlarging its indentation distance enhance voltage outputs. However, experimental results show that thickness has a greater effect than indentation distance. Beyond boosting peak voltage, increased thickness also stiffens the beam, limiting magnet oscillation amplitude and raising the natural frequency. As a result, energy dissipates more rapidly, enabling the MIMEH to reach a stable state sooner with reduced residual oscillations.

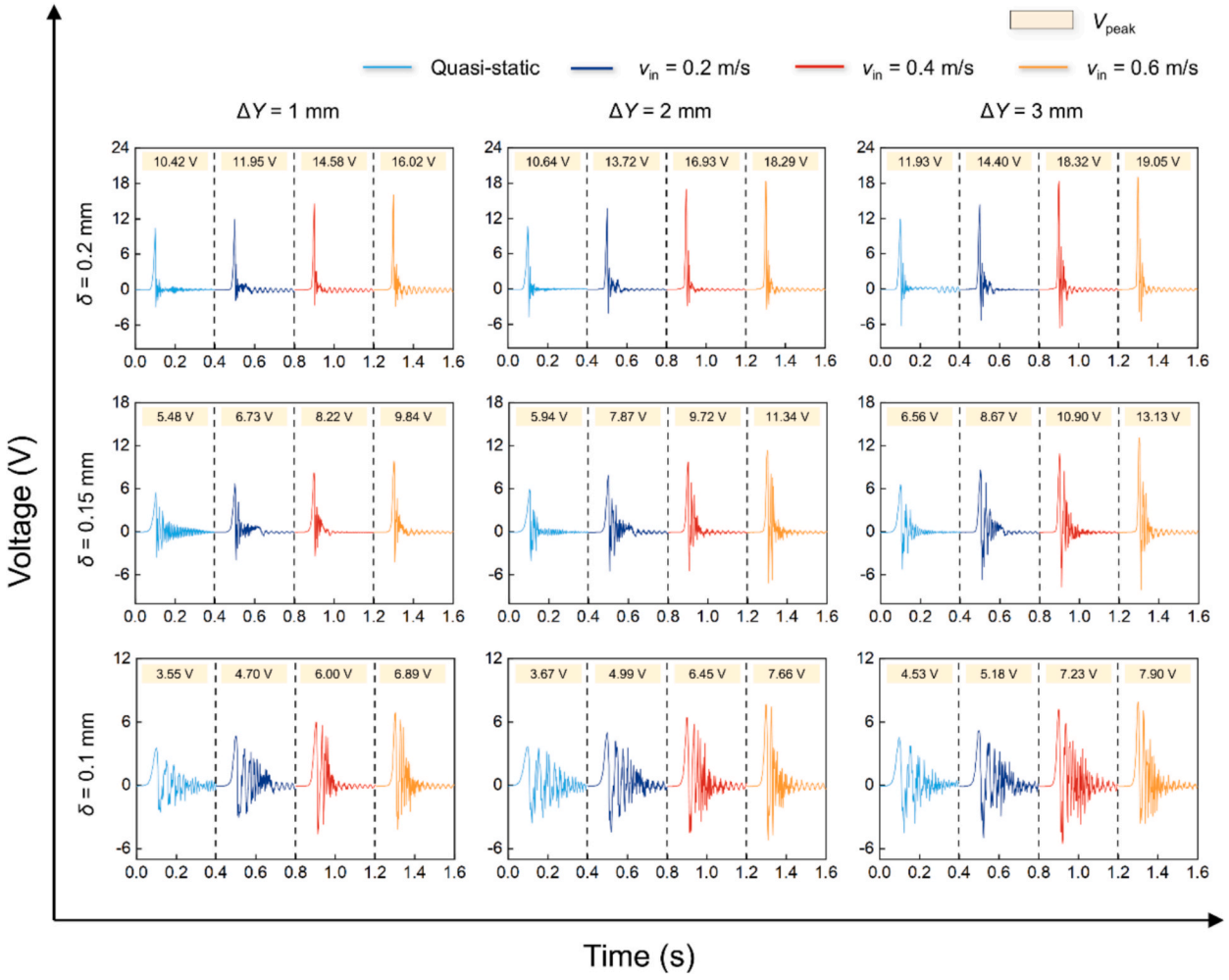

Fig. 3. Voltage output curves of MIMEHs with different bistable buckling beam thicknesses and indentation distances.

Based on the above experimental results, assembling the DiEHS using MIMEHs with thicker buckling beams is favorable from the perspective of energy harvesting. However, as indicated by Eq. (1), once the DiEHS is assembled, the magnets in each MIMEH experience not only restoring forces from their own buckling beams but also repulsive forces from adjacent modules, introducing uncertainties in the complete activation of the chain. Experiments show that when the buckling beam thickness is set to 2 mm, the initial disturbance fails to propagate fully along the DiEHS at any indentation distance tested in this study. The corresponding voltage outputs are provided in Supplementary Fig. S4. At an excitation velocity of 0.6 m/s, the repulsive force from the trigger magnet drives the first MIMEH to the position corresponding to stable state II. However, the magnet in the second MIMEH becomes trapped near the geometric center of its module, where the opposing magnetic forces from the adjacent front and rear MIMEHs nearly counterbalance each other. This equilibrium condition suppresses forward propagation, and the magnet undergoes small oscillations that quickly dissipate the input energy, thereby preventing the snap-through process from continuing. As the indentation distance of the buckling beam increases, it undergoes greater deformation, displacing the magnets in each MIMEH further from $x = 0$ (Fig. 2(a)). This strengthens the nonlinear magnetic coupling between the adjacent modules, making the second MIMEH more responsive to

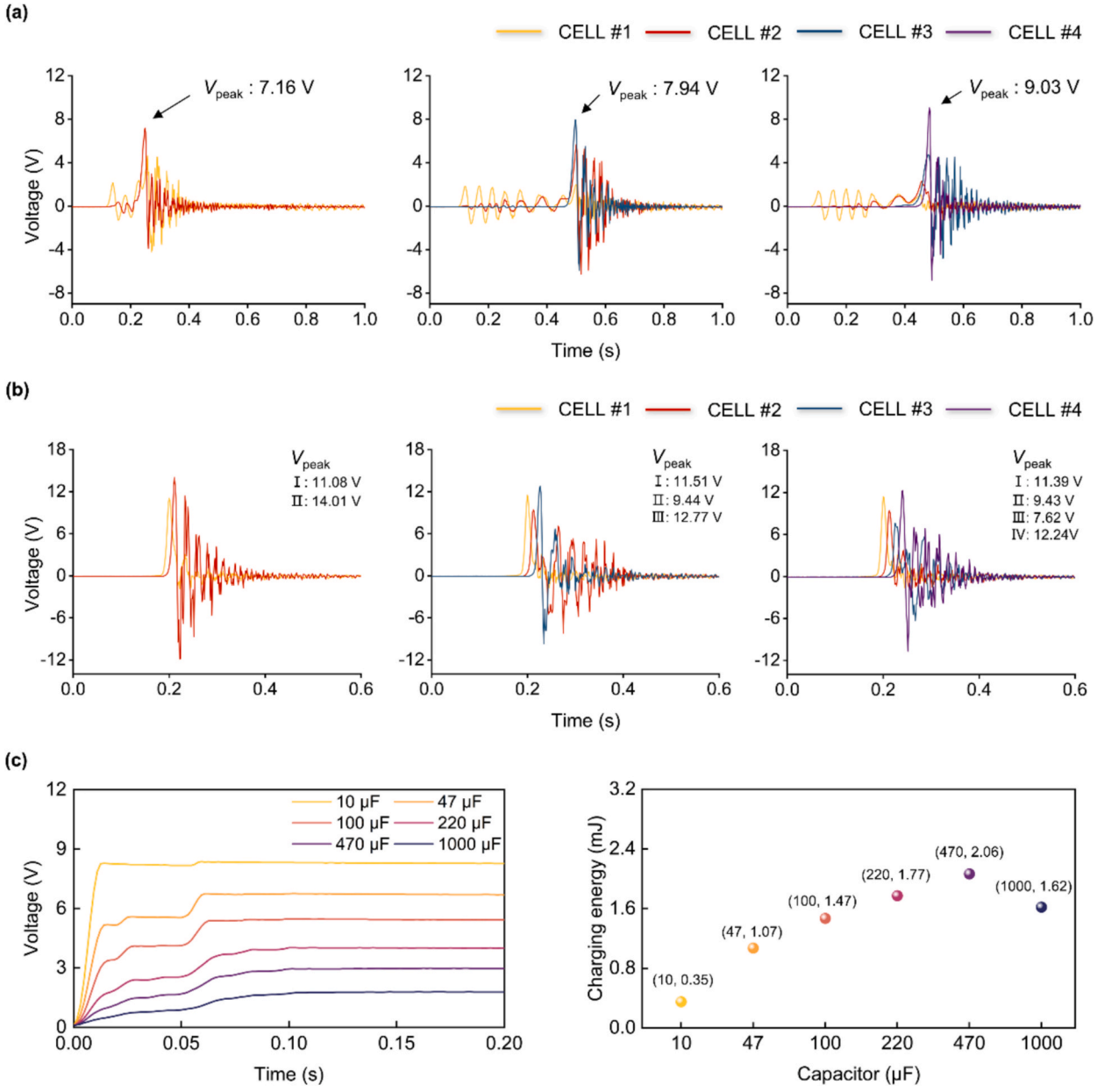

Fig. 4. (a) Voltage outputs of DiEHS with varying module numbers under quasi-static excitation. (b) Voltage outputs of DiEHS with varying module numbers under an external excitation of 0.6 m/s. (c) Charging performance of a four-module DiEHS under an external excitation of 0.6 m/s.

perturbations and exhibiting larger oscillations near the temporary equilibrium position.

To evaluate the electrical energy output of the system, a MIMEH with a 0.15 mm thick buckling beam and 3 mm indentation distance was selected as the functional tile for constructing the DiEHS. Voltage characterization and primary-pulse energy analyses were conducted on assemblies comprising two, three, and four interconnected modules. Under quasi-static excitation, results demonstrate that the output voltage of the terminal MIMEH increases with the number of modules, reaching 7.16 V, 7.94 V, and 9.03 V for the two-, three-, and four-module arrays, respectively, which correspond to increases of 9.14 %, 21.04 %, and 37.65 % compared with a single MIMEH under the same excitation conditions. In addition, each downstream module consistently produces a higher voltage than its upstream neighbor, as shown in Fig. 4(a). This indicates that the bistable potential energy stored in each MIMEH is effectively transmitted along the array, resembling the sequential toppling of dominoes.

At an increased excitation velocity of 0.6 m/s, the input energy surpassed the threshold required to trigger snap-through of the buckling beam. Each module in the DiEHS produced a distinct transient voltage pulse, indicating that a single trigger yields multiple reliable energy harvesting opportunities, whereas a single MIMEH provides only one. This capability substantially enhances the versatility and scalability of the system for downstream applications. Moreover, the output voltage of non-terminal modules gradually decreased along the propagation path, while the terminal module showed a rebound increase in voltage due to the absence of repulsion from subsequent modules, as illustrated in Fig. 4(b). Moreover, it is observed that under 0.6 m/s excitation, the first MIMEH exhibited consistent voltage across the two-, three-, and four-module arrays, and the second MIMEH output remained the same for the three- and four-module configurations. These results demonstrate that once the input energy surpasses the snap-through threshold, the voltage output of each module is governed by the local force distribution. This phenomenon offers design inspiration for vibration mitigation and protection systems that utilize chain-like sequential energy transfer mechanisms to dissipate external disturbances. The DiEHS remains functional under slight angular misalignment between the trigger and the chain. As demonstrated in Supplementary Fig. S5, a 10° lateral offset does not hinder successful activation, indicating that the system exhibits good tolerance to alignment imperfections and maintains robust triggering capability.

An energy-transfer analysis was performed for the four-module DiEHS. In evaluating the electrical output of each MIMEH, only the primary snap-through pulse was considered, as it carries the dominant portion of the mechanical energy released during the bistable transition and constitutes the component that contributes the most to powering IoT nodes. Subsequent oscillatory responses, which are highly sensitive to nonlinear interactions and largely non-transmissible to downstream modules, were excluded from the analysis. For an open-circuit voltage measurement, the maximum extractable electrical energy from a single coil can be estimated by:

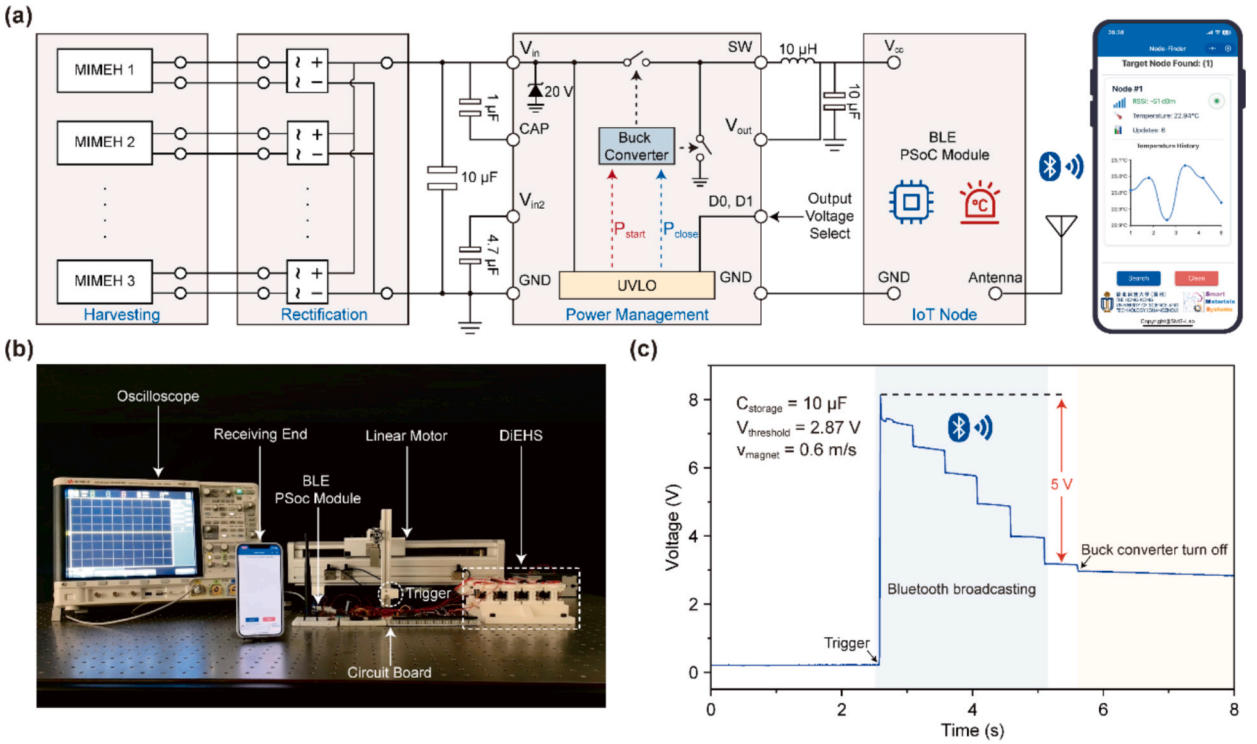

Fig. 5. (a) Schematic of the self-powered temperature-sensing system, illustrating the workflow from the DiEHS, through the rectifier, the 10 μF storage capacitor, and the energy management unit (EMU), to the IoT node with temperature sensor and Bluetooth Low Energy (BLE) module, and the receiving terminal. (b) Physical layout of the experimental platform. (c) Voltage profile across the 10 μF capacitor during system operation.

$$E_i = \int \frac{V_i^2(t)}{R_0} dt \tag{6}$$

where $V_i(t)$ is the measured open-circuit voltage, and R_0 is the coil resistance. The energy obtained from each module of the four-unit DiEHS was calculated and is plotted in Supplementary Fig. S6, showing the same trend as the measured voltage responses. To assess the practical applicability of the four-module DiEHS, repeated capacitor-charging tests were conducted using capacitances from 10 μF to 1 mF. The results from three independent trials are summarized in Supplementary Table S1. The very small variations across repeated measurements confirm the good repeatability and stability of the system. As demonstrated in Fig. 4(c), higher capacitance decreases the charging rate and reduces the final voltage. The maximum stored energy, 2.06 mJ, was achieved with a 470 μF capacitor. As compared in Supplementary Table S2, the proposed DiEHS exhibits strong application potential compared with reported electromagnetic energy harvesters in the literature.

4. Application demonstration

To demonstrate the practical potential of the DiEHS, a self-powered temperature-sensing system was developed, as demonstrated in Fig. 5(a). It incorporates the DiEHS, a rectifier bridge, a 10 μF storage capacitor, an energy management unit (EMU), an IoT node integrated with a temperature sensor and a Bluetooth Low Energy (BLE) module, and a receiving terminal. The EMU features an undervoltage lockout (UVLO) function to prevent premature power delivery and stabilize voltage output. When triggered, the DiEHS rapidly charges the storage capacitor voltage. Once the stored voltage exceeds the UVLO threshold, the EMU delivers a stable supply to the IoT node. The IoT node then activates, measures ambient temperature, and transmits the data wirelessly to the receiving terminal via BLE. As shown in Fig. 5(b) and Supplementary Video S1, after the DiEHS is triggered, the 10 μF capacitor is charged to 8.13 V within 24 ms. The wireless sensing task then begins. Fig. 5(c) shows that transmitting six temperature data points within 3 s reduces the capacitor voltage by 5.26 V, corresponding to 289.3μJ energy consumption. When the voltage drops to 2.5 V, which is below the UVLO threshold, the EMU disconnects the output, thereby cutting off power to prevent unstable operation and to protect the system.

5. Conclusion

In this study, we introduced a modular, interlocking energy harvesting mechanism. By assembling multiple bistable modules and coupling them via magnets, we developed a harvester whose dynamics resemble the cascading toppling of dominoes. This design demonstrates a robust capability to convert transient, pulse-like mechanical inputs into reliable electrical outputs. Parametric analysis of a single MIMEH unit identified the lower performance bound under varying design parameters, while array assemblies showed that voltage output scaled with module number. Notably, low-energy inputs produce progressively increasing voltages along the energy-transfer path, whereas high-energy inputs lead to sequential decreases with a rebound at the terminal module, and each module generates a distinct transient pulse that provides multiple harvesting opportunities from a single trigger. The DiEHS demonstrated excellent stability across repeated capacitor-charging tests and achieved a maximum stored energy of 2.06 mJ using a 470 μF capacitor. The system also successfully powered a wireless IoT node, highlighting its great potential for distributed sensing and self-powered applications.

CRediT authorship contribution statement

Zeye Sun: Writing – original draft, Visualization, Validation, Methodology, Investigation, Formal analysis, Data curation. **Yizhou Li:** Visualization, Investigation, Formal analysis, Data curation. **Yihao Li:** Software, Formal analysis, Data curation. **Chengyun Du:** Validation, Investigation. **Junlei Wang:** Writing – review & editing, Supervision, Project administration, Funding acquisition. **Guobiao Hu:** Writing – review & editing, Supervision, Project administration, Methodology, Funding acquisition, Formal analysis, Conceptualization.

Declaration of competing interest

The authors declare that they have no known competing financial interests or personal relationships that could have appeared to influence the work reported in this paper.

Acknowledgements

This study was partially supported by the Outstanding Youth Science Fund Rolling Support Project of Henan Province (Grant No. 252300421239), National Natural Science Foundation of China (Grant Nos. 52305135 and 52277227), Guangzhou Municipal Science and Technology Bureau (Grant Nos. SL2023A03J00869 and SL2023A04J01741), and Guangdong Provincial Project (Grant No. 2023QN10L545).

Appendix A. Supplementary data

Supplementary data to this article can be found online at https://doi.org/10.1016/j.ymssp.2025.113770.

Data availability

The data supporting this study's findings are available from the corresponding author upon reasonable request.

References

[1] W.J. Stronge, D. Shu, The domino effect: successive destabilization by cooperative neighbours, Proc. R. Soc. Lond. A 418 (1988) 155–163.
[2] T. Shi, Y. Liu, N. Wang, et al., Toppling dynamics of a mass-varying domino system, Nonlinear Dyn. 98 (3) (2019) 2261–2275.
[3] T. Shi, Y. Liu, N. Wang, et al., Toppling dynamics of regularly spaced dominoes in an array, J. Appl. Mech. 85 (4) (2018) 041008.
[4] J.M.J. van Leeuwen, The domino effect, Am. J. Phys 78 (7) (2010) 721–727.
[5] B.H. Sun, Scaling law for the propagation speed of domino toppling, AIP Adv. 10 (9) (2020) 095124.
[6] N. Nadkarni, C. Daraio, D.M. Kochmann, Dynamics of periodic mechanical structures containing bistable elastic elements: from elastic to solitary wave propagation, Phys. Rev. E 90 (2) (2014) 023204.
[7] L. Jin, R. Khajehtourian, J. Mueller, et al., Guided transition waves in multistable mechanical metamaterials, Proc. Natl. Acad. Sci. 117 (5) (2020) 2319–2325.
[8] N. Nadkarni, A.F. Arrieta, C. Chong, et al., Unidirectional transition waves in bistable lattices, Phys. Rev. Lett. 116 (24) (2016) 244501.
[9] M. Hwang, A.F. Arrieta, Extreme frequency conversion from soliton resonant interactions, Phys. Rev. Lett. 126 (7) (2021) 073902.
[10] M. Hwang, A.F. Arrieta, Topological wave energy harvesting in bistable lattices, Smart Mater. Struct. 31 (1) (2021) 015021.
[11] J.R. Raney, N. Nadkarni, C. Daraio, et al., Stable propagation of mechanical signals in soft media using stored elastic energy, Proc. Natl. Acad. Sci. 113 (35) (2016) 9722–9727.
[12] S. Yan, L.L. Wu, Y.Z. Wen, et al., Snap-through instability in mechanical metamaterials, Responsive Materials 3 (2025) e20240035.
[13] T. Yang, H.T. Xu, J. Tang, et al., Exploring nonlinear degradation benefit of bio-inspired oscillator for engineering applications, App. Math. Model. 119 (2023) 736–762.
[14] J.L. Wang, L.J. Luo, D. Yurchenko, et al., Equivalent circuit analysis of a nonlinear vortex-induced vibration piezoelectric energy harvester using synchronized switch technique, IEEE Trans. Ind. Electron. 72 (5) (2025) 4865–4876.
[15] D.K. Pan, Y. Liang, Z.M. Zhang, et al., Design and dynamics of a cantilevered bistable buckled piezoelectric beam for vibrational energy harvesting, Mech. Syst. Signal Proc. 224 (2025) 112013.
[16] S. Chiacchiari, F. Romeo, D.M. McFarland, et al., Vibration energy harvesting from impulsive excitations via a bistable nonlinear attachment-Experimental study, Mech. Syst. Signal Proc. 125 (2019) 185–201.
[17] Y.X. Cui, T. Yang, H.C. Luo, et al., Jellyfish-inspired bistable piezoelectric-triboelectric hybrid generator for low-frequency vibration energy harvesting, Int. J. Mech. Sci. 279 (2024) 109523.
[18] S. Li, L. Da Xu, S. Zhao, 5G internet of things: a survey, J. Ind. Inf. Integr. 10 (2018) 1–9.
[19] H. Heidari, O. Onireti, R. Das, et al., Energy harvesting and power management for IoT devices in the 5G era, IEEE Commun. Mag. 59 (9) (2021) 91–97.
[20] T. Sanislav, G.D. Mois, S. Zeadally, et al., Energy harvesting techniques for internet of things (IoT), IEEE Access 9 (2021) 39530.
[21] J. Wang, Z. Sun, G. Hu, et al., Improving mechanical energy harvesters without complex fabrication using origami/kirigami, Device 2 (9) (2024) 100548.
[22] X. Kang, S. Jia, Z. Lin, et al., Flexible wearable hybrid nanogenerator to harvest solar energy and human kinetic energy, Nano Energy 103 (2022) 107808.
[23] X. Kang, P. Li, Y. Wang, et al., A nonlinear galloping-driven triboelectric-electromagnetic hybrid generator for low-speed wind energy harvesting, Green Energy Intell Transp. (2025) 100363.
[24] X. Rui, H. Li, Y. Zhang, et al., An ultralow-frequency high-efficiency rotational energy harvester with bistability principle and magnetic plucking mechanism, Appl. Phys. Lett. 125 (20) (2024) 203902.
[25] Q. Zhang, C.F. Xin, F. Shen, et al., Human body IoT systems based on the triboelectrification effect: energy harvesting, sensing, interfacing and communication, Energy Environ. Sci. 15 (9) (2022) 3688–3721.
[26] B. Su, F. Guo, Z. Wang, et al., A multi-modal bidirectional galloping energy harvester with mode transition for alternating wind directions, Appl. Phys. Lett. 126 (24) (2025) 243901.
[27] Q. Zheng, L. Xin, Q. Zhang, et al., Leech-inspired amphibious soft robot driven by high-voltage triboelectricity, Adv. Mater. 37 (8) (2025) 2417380.
[28] Y. Wang, H. Du, H. Yang, et al., A rolling-mode triboelectric nanogenerator with multi-tunnel grating electrodes and opposite-charge-enhancement for wave energy harvesting, Nat. Commun. 15 (1) (2024) 6834.
[29] T.S. Zhang, L.J. Kong, Z.Y. Zhu, et al., An electromagnetic vibration energy harvesting system based on series coupling input mechanism for freight railroads, Appl. Energy 353 (2024) 122047.
[30] S. Li, P. Han, J. Wang, Enhanced energy harvesting from wake-induced rotation of an extreme light circular cylinder under the unsteady vortices, Ocean Eng. 341 (2025) 122648.
[31] Y.H. Li, Y.Z. Li, Y. Wang, et al., From nature's deadly strike to safety protection: Mantis shrimp-inspired ultrafast energy transformation for smart surveillance, Device (2025) 100903.
[32] B. Xia, X. Mei, J. Wang, Enhanced performance of piezoelectric energy harvester by installing symmetrical flexible splitter plates, Mech. Syst. Signal Proc. 225 (2025) 112257.
[33] T. Yang, J.H. Xie, Z.X. Huang, et al., Bio-inspired vibration isolator with triboelectric nanogenerator for self-powered monitoring, Mech. Syst. Signal Proc. 223 (2025) 111854.